

Article

Facilitated Unidirectional Electron Transmission by Ru Nano Particulars Distribution on MXene Mo₂C@g-C₃N₄ Heterostructures for Enhanced Photocatalytic H₂ Evolution

Qiuyu Chen ^{1,2,†} , Zonghan Huang ^{1,2,†}, Meng Liu ^{1,2}, Xiaoping Li ^{1,2} , Yuxuan Du ^{1,2}, Xiaobao Chen ^{1,2}, Dahu Ding ³, Shengjiong Yang ⁴, Yang Chen ^{1,2,*} and Rongzhi Chen ^{1,2,*} 

¹ College of Resources and Environment, University of Chinese Academy of Sciences, Beijing 100049, China; chenqiuyu20@mailsucas.ac.cn (Q.C.)

² Yanshan Earth Critical Zone and Surface Fluxes Research Station, University of Chinese Academy of Sciences, Beijing 100049, China

³ College of Resources and Environmental Sciences, Nanjing Agricultural University, Nanjing 210095, China

⁴ Key Laboratory of Environmental Engineering, Xi'an University of Architecture and Technology, No. 13, Yanta Road, Xi'an 710055, China

* Correspondence: chenyang@ucas.ac.cn (Y.C.); crz0718@ucas.ac.cn (R.C.)

† These authors contributed equally to this work.

Abstract: Precious metals exhibit promising potential for the hydrogen evolution reaction (HER), but their limited abundance restricts widespread utilization. Loading precious metal nanoparticles (NPs) on 2D/2D heterojunctions has garnered considerable interest since it saves precious metal consumption and facilitates unidirectional electron transmission from semiconductors to active sites. In this study, Ru NPs loaded on MXenes Mo₂C by an in-site simple strategy and then formed 2D/2D heterojunctions with 2D g-C₃N₄ (CN) via electrostatic self-assembly were used to enhance photocatalytic H₂ evolution. Evident from energy band structure analyses such as UV-vis and TRPL, trace amounts of Ru NPs as active sites significantly improve the efficiency of the hydrogen evolution reaction. More interestingly, MXene Mo₂C, as substrates for supporting Ru NPs, enriches photoexcited electrons from CN, thereby enhancing the unidirectional electron transmission. As a result, the combination of Ru-Mo₂C and CN constructs a composite heterojunction (Ru-Mo₂C@CN) that shows an improved H₂ production rate at 1776.4 μmol·g⁻¹·h⁻¹ (AQE 3.58% at 400 nm), which is facilitated by the unidirectional photogenerated electron transmission from the valence band on CN to the active sites on Ru (CN→Mo₂C→Ru). The study offers fresh perspectives on accelerated unidirectional photogenerated electron transmission and saved precious metal usage in photocatalytic systems.

Keywords: metal nanoparticles; MXene Mo₂C; graphite carbon nitride; unidirectional electronic transmission; hydrogen evolution



Citation: Chen, Q.; Huang, Z.; Liu, M.; Li, X.; Du, Y.; Chen, X.; Ding, D.; Yang, S.; Chen, Y.; Chen, R. Facilitated Unidirectional Electron Transmission by Ru Nano Particulars Distribution on MXene Mo₂C@g-C₃N₄ Heterostructures for Enhanced Photocatalytic H₂ Evolution. *Molecules* **2024**, *29*, 1684. <https://doi.org/10.3390/molecules29071684>

Academic Editors: M. Shaheer Akhtar and Md. Abu Hanif

Received: 17 March 2024

Revised: 7 April 2024

Accepted: 8 April 2024

Published: 8 April 2024



Copyright: © 2024 by the authors. Licensee MDPI, Basel, Switzerland. This article is an open access article distributed under the terms and conditions of the Creative Commons Attribution (CC BY) license (<https://creativecommons.org/licenses/by/4.0/>).

1. Introduction

The use of semiconductor photocatalysis for hydrogen generation is a hopeful solution for the issues of energy scarcity and pollution [1–3]. However, the efficiency of electronic-hole pair separation and reduction reaction kinetics in surface water are crucial issues that impact photocatalytic hydrogen production [4–6]. Various techniques, such as morphology modulation, valence band potential engineering, and heterogeneous structure building, have been utilized to address the aforementioned key problems [7–10]. Precious metals, notably platinum (Pt), are recognized for their efficacy as co-catalysts to form heterojunctions with semiconductors by lowering the overpotentials required for surface water reduction reactions and enhancing charge transmission [11]. Nevertheless, the limited availability and elevated costs hinder the widespread application of precious

metals as co-catalysts [12,13]. Hence, there has been a growing focus in recent years on minimizing the amount of precious metal co-catalysts used in photocatalytic hydrogen generation [14,15].

Ruthenium (Ru), a relatively cost-effective metal from the platinum group, has Ru-H bond strengths comparable to those of Pt-H bonds, which suggests that it could be a viable substitute for Pt [16,17]. To save on the use of precious metals, many studies have attempted to load Ru nanoparticles (NPs) onto other co-catalysts [18,19]. Ru NPs can change the electronic structure of heterojunctions and introduce abundant active sites, resulting in several times the hydrogen production performance of the original catalyst [20,21]. Incorporating Ru NPs onto two-dimensional (2D) structures, such as g-C₃N₄, is more achievable for the uniform distribution of active sites due to the extensive expanse of surface area [22,23].

2D g-C₃N₄ is an ideal semiconductor photocatalyst because of its stable physicochemical properties and suitable band gap [24]. Nevertheless, the extensive use of pure g-C₃N₄ in photocatalysis is limited due to its slow charge transfer rate and rapid complexation of photoexcited electron-hole pairs [25]. To address the mentioned issues, MXene Mo₂C with superior conductivity can create a 2D/2D heterostructure with g-C₃N₄ [26], with chemical bonds and van der Waals force accelerating electron migration, thus greatly facilitating the catalytic reaction [27]. Furthermore, Mo₂C exhibits excellent metal-like conductivity and a lower valence band position to form a Schottky junction with CN, thereby promoting the directional migration of photogenerated electrons via the junction [28]. The metalloid's conductivity can be attributed to its Pt-like d-orbital structure, which is created by hybridizing Mo d-orbitals with C s/p-orbitals [29]. However, the higher bond energy of the Mo-H bond (65–75 kcal mol⁻¹) in Mo₂C MXene results in robust adsorption of H⁺ ions, hence exhibiting limited desorption of H₂ molecules from the Mo atoms [30,31]. Therefore, it is essential to incorporate hydrogen evolution reaction (HER) activity into Mo₂C to establish a balance in atomic hydrogen adsorption and desorption for improving photocatalytic hydrogen production [32].

This research combines a Ru-doped 2D MXene Mo₂C co-catalyst with 2D g-C₃N₄ layers to improve their hydrogen evolution efficiency. The conductive Mo₂C enriches the photogenerated electrons generated in CN through the Schottky junction, as evidenced by time-resolved photoluminescence (TRPL) and electrochemical impedance spectroscopy (EIS). In addition, based on energy band structure analysis and the UV-Vis absorbance spectrum (UV-Vis), the active sites introduced by Ru NPs at the interface enhance the surface water reduction reaction, thereby guiding the enriched electrons to Ru. The Schottky barriers between Mo₂C and CN inhibit the reverse flow and recombination of electron-hole pairs, thus facilitating unidirectional electron transmission from the semiconductor to the active sites (CN → Mo₂C → Ru). As anticipated, the Ru-Mo₂C@g-C₃N₄ heterostructure demonstrated a notable hydrogen production rate of 1776.4 μmol·g⁻¹·h⁻¹ and an apparent quantum efficiency (AQE) of 3.58% at 400 nm, surpassing the majority of reported Mo₂C/g-C₃N₄ photocatalytic systems. This study presents a strategy for unidirectional electron migration by loading trace precious metal NPs, which provides guidance for improving charge migration efficiency in photocatalytic hydrogen production.

2. Results and Discussion

2.1. Construction Strategy of Ru-Mo₂C@CN

The production of Ru-Mo₂C@CN photocatalysts followed the specific procedure outlined in Figure 1. Briefly, 2D MXene Mo₂C was prepared by etching Mo₂Ga₂C with HCl-LiF in hydrothermal conditions, while Ru/Mo₂C was fabricated by etching Mo₂Ga₂C with HCl-LiF-RuCl₃. In the second step, Ru³⁺ in the solution is transformed into Ru clusters attached to the Mo₂C surface, with Ga being oxidized and subsequently eliminated. This redox reaction occurs spontaneously from a thermodynamic perspective. The Ru-Mo₂C@CN was eventually formed via the electrostatic self-assembly of 2D g-C₃N₄ nanosheets and MXene Ru-Mo₂C layers.

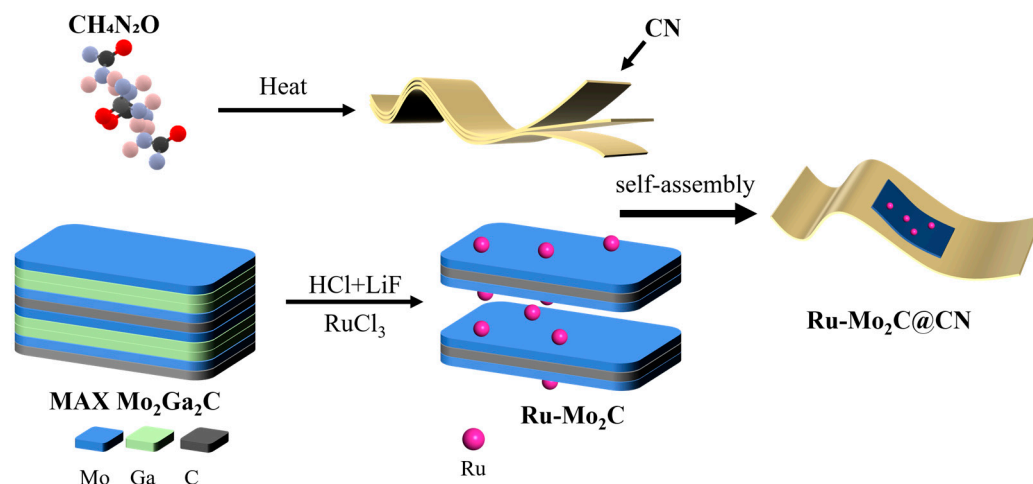


Figure 1. Simplified synthesis diagram of Ru-Mo₂C@CN.

2.2. Synthesis and Structural Morphology of Ru-Mo₂C@CN

The MXene Mo₂C without Ru loading exhibits a typical layered structure, which will help prevent the aggregation of Ru nanoparticles (Figure S1). The scanning electron microscope (SEM) images (Figure 2a,b) displayed that the Ru-Mo₂C nanosheets showed a flat and smooth 2D structure after etching, while the CN nanosheets showed a reticulated 2D structure, which created the possibility of electrostatic self-assembly between the two. High-resolution transmission electron microscopy (HRTEM) revealed the surface morphology, indicating the existence of Ru NPs in Figure 2c,d. As shown in Figure 2c, Ru supported on the Mo₂C surface consists of nanoparticles smaller than 5 nm, which provide more abundant catalytic active sites for photocatalytic reactions compared with Ru clusters. The HRTEM image in Figure S2 also proves this conclusion. From the HRTEM image of Figure 2d, the Ru-Mo₂C@CN is assembled from Mo₂C nanosheets loaded with Ru NDs and 2D g-C₃N₄ nanosheets. Furthermore, as shown in Figure 2e–h, energy dispersive X-ray spectroscopy (EDX) analysis indicated that Ru NPs are uniformly dispersed on the Mo₂C surface. The above characterization indicates that MXene can serve as a carrier for the highly dispersed loading of precious metals. Even if the amount of precious metals added is small, they can uniformly adhere to the surface of MXene.

The absence of typical metallic Ru phase peaks in the XRD scan of MXene could be attributed to the limited presence of Ru content on the surface (Figure 3a), falling below the detection threshold, or because the Ru grains are too small on the surface of MXene to be diffracted during the X-ray diffraction (XRD) scanning. In addition, the (002) diffraction peak of Mo at 8.6° is somewhat shifted due to the introduction of Ru [33]. The shifted peaks showed that Ru clusters disrupt the integrity of the lattice. X-ray photoelectron spectrometer (XPS) analysis provides additional details on the surface chemical properties of the Ru-Mo₂C@CN photocatalyst. The N 1s spectra display three distinct peaks at 401.9, 400.2, and 398.7 eV, corresponding to terminal amino groups (C-N-H_x), tertiary nitrogen (N-C₃), and sp²-hybridized nitrogen (C=N-C), as described in references [34,35]. Ru-Mo₂C@CN shows a positive shift in the typical peaks of the N spectra compared to CN, suggesting unidirectional electron transmission from CN to Ru-Mo₂C.

This finding indicates that the close connections between Mo₂C and CN could offer a successful route for electron transfer. Surprisingly, the XPS data (Table S1) showed that Ru NPs accounted for only 0.5% of the total surface elements in the Ru-Mo₂C@CN, indicating that trace amounts of NPs can significantly reduce the dependence of HER on noble metals. The peaks at 484.3 and 462.1 eV in the Ru 3p spectra of Ru-Mo₂C and Ru-Mo₂C@CN are indicative of the Ru 3p_{3/2} and 3p_{1/2} associated with metallic Ru⁰ [36,37], indicating the successful Ru NPs deposition on Mo₂C (Figures 3d and S3). The Mo 3d spectrum of the Ru-Mo₂C@CN sample (Figure 3e) can be deconvoluted into six peaks, which confirms the presence of Mo⁴⁺, Mo⁵⁺, and Mo⁶⁺ species. The peaks at 229.7 (3d_{5/2}) and 232.9 eV (3d_{3/2})

are attributed to Mo^{4+} ions, and the peaks observed at 233.0 ($3d_{5/2}$) and 236.2 ($3d_{3/2}$) belong to Mo^{6+} ions [38,39], due to the partial oxidation of Mo_2C . Additionally, the sub-oxide Mo^{5+} peaks, which appear at 230.9 ($3d_{5/2}$) and 234.0 eV ($3d_{3/2}$), may contribute to the X-ray reduction of Mo^{6+} in XPS tests [40,41]. More importantly, the Mo 3D spectrum of Ru- $\text{Mo}_2\text{C}@$ CN exhibits a significant negative shift in comparison to the XPS spectra of the original Ru- Mo_2C . The noticeable change is due to the successful interfacial interaction between the MXene Mo_2C and the CN nanosheets, resulting in a decrease in the bond strength of Mo-H in Ru- $\text{Mo}_2\text{C}@$ CN and boosting HER performance [42,43].

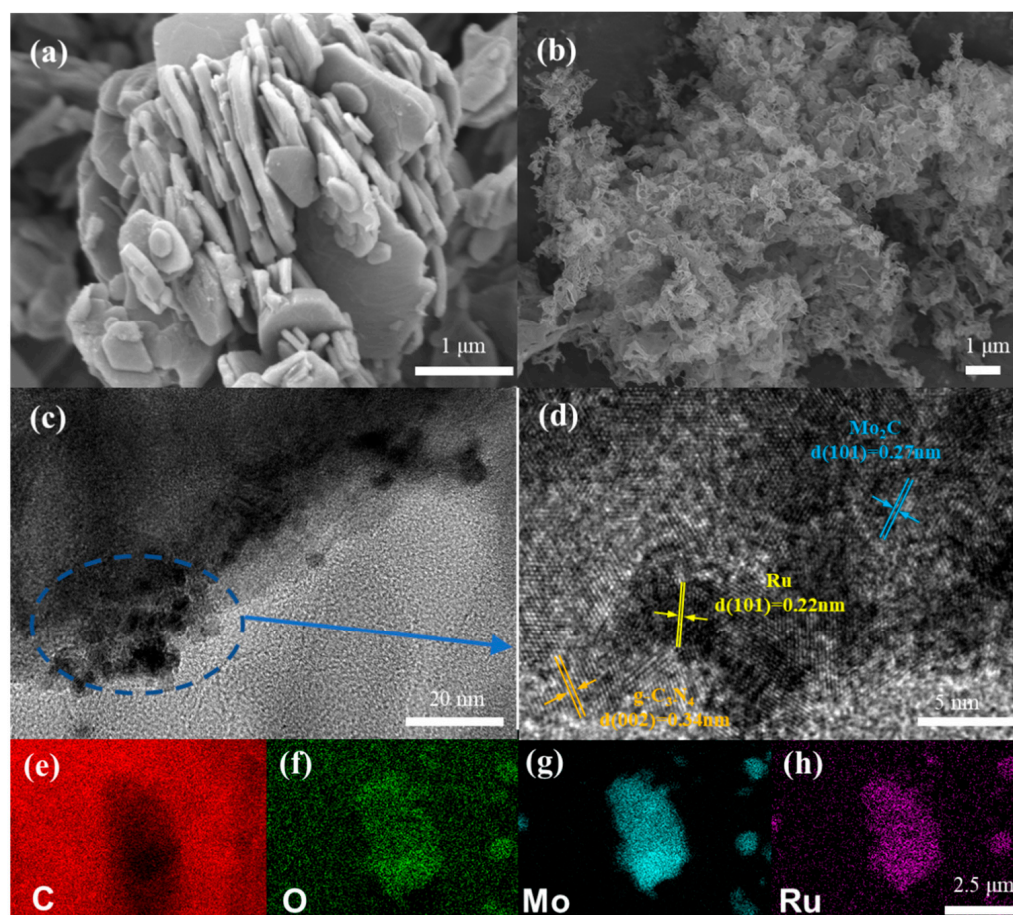


Figure 2. Analysis of the microstructure and morphology of Ru- Mo_2C . (a) Ru- Mo_2C SEM image; (b) 2D structure of CN SEM image; (c,d) HRTEM images; (e–h) EDX elemental mappings.

The Fourier transform infrared spectroscopy (FTIR) of Figure 3f suggests that both $\text{Mo}_2\text{C}@$ CN and Ru- $\text{Mo}_2\text{C}@$ CN photocatalysts exhibit comparable characteristic peaks to CN. Two separate peaks around 806 and 884 cm^{-1} are likely caused by the vibrational modes related to the triazine units' breathing. Previous studies support the conclusion that triazine units are the primary molecular composition of CN materials, making this observation highly convincing [44]. A broadband was observed in the 1233 – 1637 cm^{-1} region, which can be attributed to CN heterocyclic stretching vibration. In addition, the peaks at approximately 1243 , 1330 , 1412 , 1464 , 1572 , and 1635 cm^{-1} are indicative of the presence of C-N bonds and C=N bond structures in the catalyst [44,45]. A group of high points can be seen in the spectrum between 3068 and 3524 cm^{-1} , likely caused by the absorption of water molecules and subsequent stretching vibrations of N-H bonds [46]. The appearance of spectral characteristic peaks of g- C_3N_4 in the above-mentioned composite materials confirms that Mo_2C doping does not damage the structure of CN.

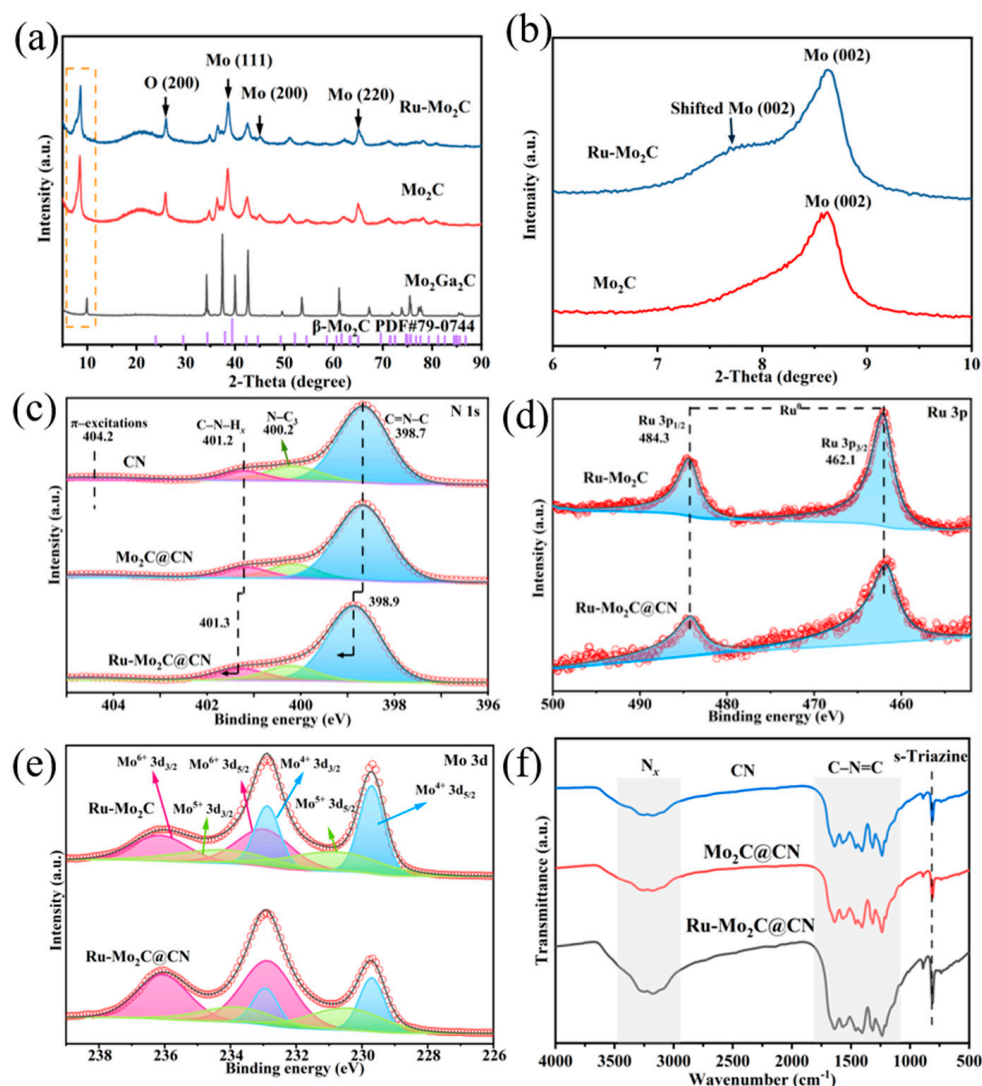


Figure 3. Analysis of Ru-Mo₂C through structural and spectroscopic characterization. (a) XRD patterns of Mo₂Ga₂C, Mo₂C, and Ru-Mo₂C. (b) Enlarged Mo (002) diffraction peaks. High-resolution XPS spectra of (c) N 1s, (d) Ru 3p, and (e) Mo 3d. (f) FTIR spectra of CN, Mo₂C@CN, and Ru-Mo₂C@CN.

2.3. Photocatalytic Performance

As shown in Figure 4a, the rapid rate of electron-hole pair complexation in CN leads to a low rate of H₂ production through photocatalysis, with only minimal amounts of H₂ detectable after 2 h of illumination. The combination of Mo₂C and CN significantly increases the H₂ production rate to 129.9 μmol·g⁻¹·h⁻¹ by providing electron transfer pathways and reducing the recombination of photo-generated electron-hole pairs. The increase in hydrogen production rate indicates that Mo₂C can serve as a co-catalyst to improve the efficiency of H₂ production in CN. Due to the large particle size of the bulk Mo₂C, it could not be fully combined with CN. Therefore, a two-dimensional structure of Mxene Mo₂C was chosen to bind with CN in this study. Substituting Mxene Mo₂C for the original Mo₂C in the composite material resulted in a renewed increase in the rate of photocatalytic H₂ production to 271.5 μmol·g⁻¹·h⁻¹, demonstrating that the 2D/2D pairing effectively enhanced the movement of photogenerated carriers, leading to a decrease in carrier recombination rate. It is common knowledge that Ru has emerged as a viable alternative to Pt for generating hydrogen through photocatalysis. The photocatalytic H₂ production performance of composite materials was further enhanced by doping 2D Mo₂C

with Ru. After introducing 0.5% Ru into Mo₂C@CN, the photocatalysts reached a hydrogen production rate of 1776.4 $\mu\text{mol}\cdot\text{g}^{-1}\cdot\text{h}^{-1}$ and exhibited an apparent quantum yield (AQE) of 3.58% at 400 nm (detailed calculations in attachment), surpassing the performance of most reported Mo₂C/g-C₃N₄ photocatalysts (Table S2). Importantly, to determine the successful construction of the heterojunction, we simply milled 10 mg of Ru-Mo₂C with 90 mg of CN to obtain a physically mixed sample labeled Ru-Mo₂C + CN. It was found that the hydrogen production rate of Ru-Mo₂C + CN was much lower than that of Ru-Mo₂C@CN, which can also be taken as evidence that the Ru-Mo₂C@CN heterojunction was successfully constructed via electrostatic self-assembly (Figure S4). This excellent performance indicates that the 2D structure of Mo₂C can serve as a good co-catalyst to improve the migration rate of photogenerated carriers, thereby further reducing the carrier complexation rate. In addition, the 2D structure of Mo₂C can serve as a good intermediate carrier, providing more coverage areas for Ru as an active site.

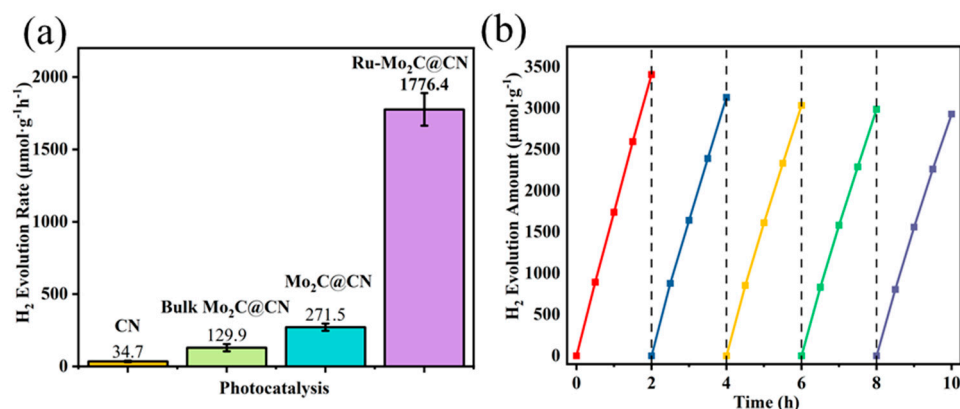


Figure 4. (a) The H₂ evolution efficiency of all photocatalysts; (b) stability test of Ru-Mo₂C@CN.

Furthermore, it is crucial to consider the durability of the photocatalytic process, as demonstrated in Figure 4b, which illustrates the hydrogen generation rate by Ru-Mo₂C@CN during a 10-h hydrogen production cycle. The photocatalyst showed good recyclability, as its hydrogen production rate decreased by less than 20% after five cycles. As shown in Figure S5, XRD images of the Ru-Mo₂C@CN photocatalyst remain consistent before and after five cycles, indicating its good stability.

2.4. Photocatalytic Mechanism Analysis

To understand why the photocatalytic performance improved, the light absorption abilities of various photocatalysts were initially examined using UV-Vis. As shown in Figure 5a, the intrinsic absorption edges of Ru-Mo₂C@CN redshift to 493 nm, compared to the original CN's inherent absorption edge at 468 nm. The redshift phenomenon is due to the strong visible light absorption ability of the Mo₂C co-catalyst, indicating that Mo₂C can promote the unidirectional electronic transmission from CN to Ru-Mo₂C. Compared with Mo₂C@CN, the absorbance of the photocatalyst can be slightly improved in the case of Ru-Mo₂C doping, which indicates that Ru NPs as a co-catalyst can enhance the light-harvesting ability of composite materials. In addition, the overall absorbance of Ru-Mo₂C@CN showed a significant improvement, which may be related to the influence of Ru clusters on the Mo lattice.

As shown in Figure 5b, Kubelka–Munk functional plots of three photocatalysts were obtained based on the UV-visible photometric spectral transformation. The bandgap value of Ru-Mo₂C@CN (2.37 eV) is slightly lower than that of Mo₂C@CN (2.40 eV) and much lower than that of CN (2.52 eV), which demonstrates the formation of a Schottky junction between Mo₂C and CN, leading to a decrease in the bandgap. CN has a higher bandgap value of 2.52 eV compared to Mo₂C@CN with 2.40 eV, whereas Ru-Mo₂C@CN has a lower bandgap value of 2.37 eV. The difference in bandgap can be attributed to the close contact

between Mo₂C and CN, which generates Schottky junctions and decreases the bandgap of Mo₂C@CN and Ru-Mo₂C@CN. Furthermore, the reduction in the band gap suggests that the presence of a Mo₂C co-catalyst enhances the ability of CN to be stimulated by visible light, aligning with the enhanced photocatalytic efficiency of Ru-Mo₂C@CN.

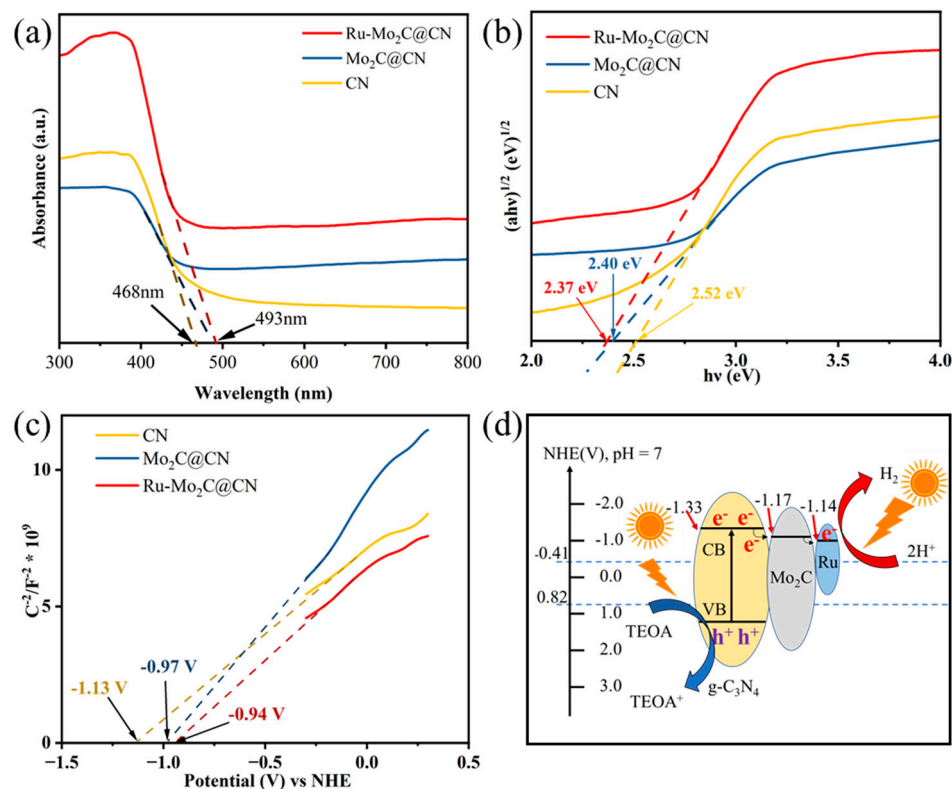


Figure 5. (a) UV-vis absorbance spectrum of CN, Mo₂C@CN, and Ru-Mo₂C@CN photocatalysts. (b) Tauc plots of three photocatalysts. (c) Mott–Schottky (M-S) curves of three photocatalysts (200 Hz). (d) Band structure schematic of the Ru-Mo₂C@CN composite.

To explore the effect of Mo₂C on the semiconductor band gap, M-S measurements of the prepared catalyst were performed at a frequency of 200 Hz (Figure 5c). To find the flat band potential (E_{FB}), extend the linear part of the M-S graph to the x-axis and locate the point where it intersects. In addition, the intercepts of the three catalysts in the M-S plot are all positive, indicating the characteristics of their n-type semiconductors [47]. Generally speaking, the conduction band potential (E_{CB}) of n-type semiconductors is 0.2 eV greater than the E_{FB} [48]. Therefore, the E_{CB} for CN, Mo₂C@CN, and Ru-Mo₂C@CN concerning the Normal Hydrogen Electrode (NHE) are -1.33 , -1.17 , and -1.14 V, respectively. Based on the preceding results, Figure 5d illustrates the band structure of Ru-Mo₂C@CN. When exposed to light, a large quantity of photoexcited electrons are produced within CN and jump into the conduction band (CB). Photoexcited electrons from CN are moved to Mo₂C with a lower CB via the Schottky junction, then quickly transferred to Ru NPs for the reaction with H⁺ at the active site to produce hydrogen gas. The 0.16 V Schottky barriers between the CB of Mo₂C and CN promote unidirectional electron migration.

To better understand the complexation process of photoexcited electron-hole pairs, photoluminescence (PL) spectra and TRPL spectra were used to analyze carriers' behavior. Figure 6a shows the PL spectra of CN, Mo₂C@CN, and Ru-Mo₂C@CN. Due to electronic transitions between bands, each photocatalyst exhibits a distinct emission peak at approximately 470–490 nm under excitation at 325 nm, which is consistent with previous research results. Mo₂C@CN exhibits lower PL intensity than CN, indicating successful suppression of electron-hole recombination through rapid charge transfer from CN to Mo₂C. The Ru-Mo₂C@CN composite shows a slightly elevated PL intensity compared to

Mo₂C@CN, accompanied by a significant peak redshift. This observation suggests that the Ru NPs may act as catalytic sites for HER, thereby enhancing the production rate of electron-hole pairs within the system, which is consistent with the results of UV-vis testing. The more electron-hole pairs are generated, the more electron-hole pairs are recombined, ultimately leading to higher PL intensity. As shown in Figure 6b, the TRPL spectra of the prepared catalyst all conform to double exponential fitting (detailed data in Table S3). Among them, τ_1 denotes the duration of fluorescence decay for electrons transitioning from the conduction band to the valence band of CN, while τ_2 denotes the duration of fluorescence decay for the recombination of electron-hole pairs generated by light on the CN. The average fluorescence lifetime of the TRPL spectra was calculated by the following equation [49]:

$$\tau = (A_1\tau_1^2 + A_2\tau_2^2) / (A_1\tau_1 + A_2\tau_2)$$

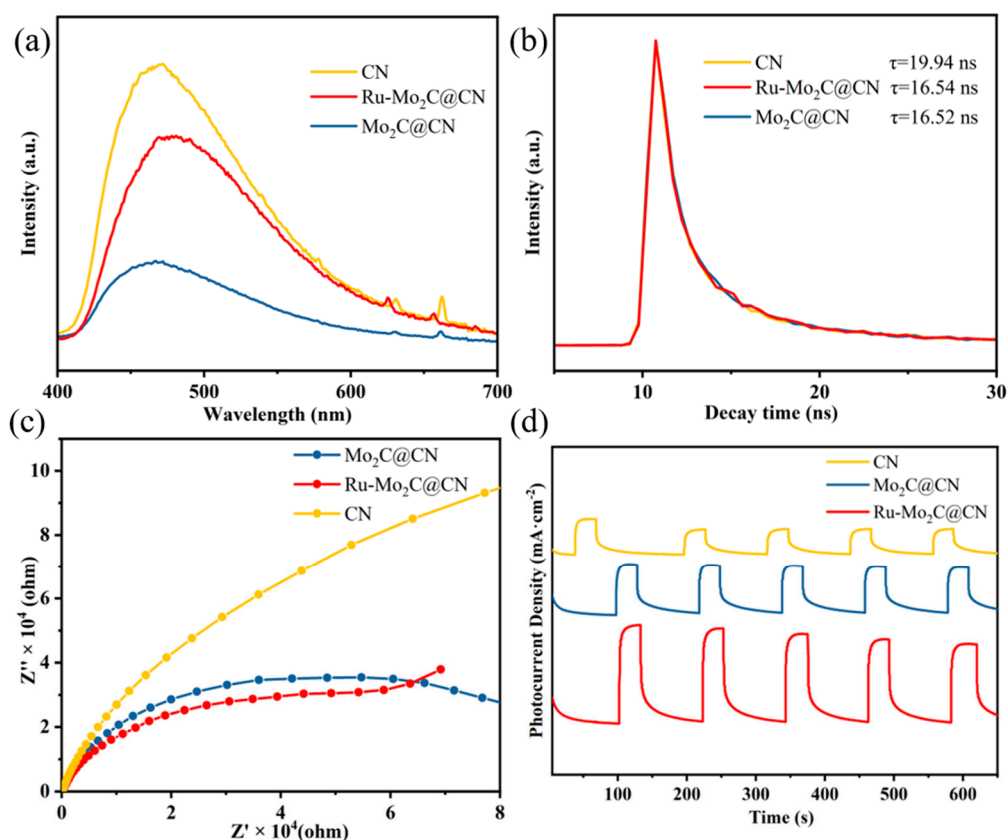


Figure 6. (a) PL and (b) TRPL spectra of three photocatalysts. (c) EIS Nyquist plots and (d) transient photocurrent plots of three photocatalysts.

Following the addition of Mo₂C co-catalysts, both τ_2 and τ were significantly reduced, whereas the presence of Ru NPs had a minimal impact on τ_2 and τ . The decreased duration of τ_2 could be attributed to the quick transfer of electrons at the interface from the CN in an excited state to Mo₂C. Further, Ru NPs barely affect the electron transfer rate.

To further investigate the effect of Ru-Mo₂C on the interfacial electron migration rate in ternary catalysts, we used photoelectrochemical (PEC) detection to investigate the effect of Mo₂C and Ru NPs on the migration rate of photogenerated electrons. The Nyquist plot of the EIS was conducted to analyze the characteristics of charge transfer resistance (Figure 6c), in which the resistance of all photocatalysts exhibited similar semicircle curves [50]. The Ru-Mo₂C@CN has the smallest arc radius, indicating the lowest resistance to charge transfer at the interface, which aligns with its superior photocatalytic activity. Moreover, compared with CN, Mo₂C@CN and Ru-Mo₂C@CN samples show higher photocurrent density (Figure 6d), indicating that the introduction of Mo₂C improved the rate of electron

generation and migration. Linear sweep voltammetry (LSV) can further demonstrate the functions of Ru-Mo₂C as a co-catalyst in the photocatalytic process. As shown in Figure S6, the Ru-Mo₂C@CN photocatalyst exhibits enhanced cathode current and a more advantageous potential in comparison to CN and Mo₂C@CN. This indicates that Ru NPs can enhance the surface reaction [51]. These results indicate that the Mo₂C in Ru-Mo₂C@CN can increase the rate of electron generation and migration, while the Ru on the surface can serve as an active site to significantly enhance the reduction effect of H⁺ in hydrogen production reactions [52].

3. Experimental Section

3.1. Materials

All reagents, including dicyandiamide (C₂H₄N₄), urea (CH₄N₂O), melamine, lithium fluoride (LiF), ruthenium chloride trihydrate (RuCl₃·3H₂O), molybdenum gallium carbon (Mo₂Ga₂C), ammonium molybdate tetrahydrate ((NH₄)₆Mo₇O₂₄·4H₂O), triethanolamine (TEOA), ethanol, hydrochloric acid (HCl), ammonia (liquid), and deionized (DI) water, are analytically pure.

3.2. Preparation of Photocatalysts

3.2.1. Preparation of 2D g-C₃N₄ Nanosheets (CNs)

2D g-C₃N₄ nanosheets were prepared using urea as a precursor. According to the existing methods of our group [53], a ceramic crucible was filled with 25 g of urea, covered with a lid, then heated in a muffle furnace at a heating rate of 5 °C·min⁻¹ until reaching 550 °C and maintained for 4 h. After cooling to room temperature, the resulting material was transferred to another ceramic crucible, heated again in the furnace at the same rate to 500 °C, and kept for 2 h. The final product, 2D g-C₃N₄ nanosheets, was obtained after grinding and labeling CN.

3.2.2. Preparation of MXene Mo₂C (Mo₂C) and Ru-Doped Mo₂C (Ru-Mo₂C)

1 g of LiF and 0.8 g of Mo₂GaC were added to the inner tank of the reactor, then 30 mL of an 8 M HCl solution was added to the inner tank of the reactor and stirred for 12 h. Then, heat the reactor in a 180 °C oven for 24 h. After natural cooling to room temperature, let it stand for 8 h to obtain the black solid. Wash the black solid with water and ethanol again, and centrifuge three times to obtain the bottom sediment. Finally, the bottom sediment was placed in a vacuum drying oven at 50 °C and dried for 8 h to obtain MXene Mo₂C.

Ru-Mo₂C was prepared in the same conditions as Mo₂C. Differently, put 1 g of LiF, 0.8 g of Mo₂Ga₂C, and 40 mg of RuCl₃·3H₂O into the inner tank of the reactor before adding 30 mL of an 8 M hydrochloric acid solution. The remaining steps are identical to preparing Mo₂C.

3.2.3. Preparation of Bulk Mo₂C

A total of 1.18 g of (NH₄)₆Mo₇O₂₄·4H₂O was taken with 210 mg of C₂H₄N₄ and fully milled. Subsequently, the mixture was transferred into a tube furnace and subjected to heating at a rate of 5 °C·min⁻¹ in the N₂ atmosphere condition until reaching a temperature of 750 °C, where it was maintained for 8 h. Following the natural cooling process to ambient temperature, thoroughly grind and calcine the product to obtain bulk Mo₂C.

3.2.4. Preparation of MXene Mo₂C@CN, Bulk Mo₂C@CN, and Ru-Mo₂C@CN Composites

10 mg of different Mo₂C species and 90 mg of CN nanosheets were dispersed in 40 mL of an aqueous solution containing 50% ethanol and stirred overnight. The solid particles were separated through centrifugation, rinsed with deionized water, and subsequently desiccated in a vacuum oven to obtain MXene Mo₂C@CN, bulk Mo₂C@CN, and Ru-Mo₂C@CN, respectively.

3.3. Characterization and Experimentation

The characterization of samples, photocatalytic hydrogen evolution tests, and photoelectrochemical measurements are detailed in the Supplementary Materials.

4. Conclusions

In summary, Ru NPs were loaded onto Mxene Mo₂C in situ for constructing ternary catalysts of Ru-Mo₂C@CN via electrostatic self-organization for enhancing hydrogen production. The introduction of trace amounts of Ru NPs on Mo₂C with good conductivity can significantly improve photocatalytic hydrogen production performance and effectively reduce the dependence of photocatalytic hydrogen production systems on rare and precious metals. In addition, the 2D/2D Schottky junction formed by Mo₂C and CN, along with the presence of abundant active sites facilitated by Ru, enhances the unidirectional electronic transmission, consequently mitigating the backflow and recombination of electron-hole pairs. As expected, in the presence of a TEOA sacrificial agent, the Ru-Mo₂C@CN catalyst can achieve a high H₂ production rate of 1776.4 μmol·g⁻¹·h⁻¹ with an AQE value of 3.58% at 400 nm. These results present a new potential approach to achieve trace loading for scarce precious metals and regulate charge transport pathways.

Supplementary Materials: The following supporting information can be downloaded at: <https://www.mdpi.com/article/10.3390/molecules29071684/s1>. References [54–59] are cited in the Supplementary Materials.

Author Contributions: Conceptualization, Q.C., Z.H. and R.C.; methodology, Q.C., Z.H., X.L. and X.C.; investigation, Q.C., Z.H., M.L. and Y.D.; data curation, Q.C., Z.H. and M.L.; writing—original draft preparation, Q.C. and Z.H.; writing—review and editing, Q.C., Z.H., M.L., X.L., Y.D., X.C. and R.C.; supervision, D.D. and S.Y.; funding acquisition, Y.C. and R.C. All authors have read and agreed to the published version of the manuscript.

Funding: This research was funded by the National Natural Science Foundation of China (No. 42277243), the National Key Research and Development Program of China (No. 2022YFC3902300), the Guangdong Foundation for Program of Science and Technology Research (No. 2020B1212060053), and the Fundamental Research Funds for the Central Universities.

Institutional Review Board Statement: Not applicable.

Informed Consent Statement: Not applicable.

Data Availability Statement: Data are contained within the article and Supplementary Materials; further inquiries can be directed to the corresponding author.

Conflicts of Interest: The authors declare no conflicts of interest.

References

1. Hisatomi, T.; Domen, K. Reaction Systems for Solar Hydrogen Production Via Water Splitting with Particulate Semiconductor Photocatalysts. *Nat. Catal.* **2019**, *2*, 387–399. [CrossRef]
2. Wang, Q.; Domen, K. Particulate Photocatalysts for Light-Driven Water Splitting: Mechanisms, Challenges, and Design Strategies. *Chem. Rev.* **2020**, *120*, 919–985. [CrossRef] [PubMed]
3. Chandrasekaran, S.; Yao, L.; Deng, L.; Bowen, C.; Zhang, Y.; Chen, S.; Lin, Z.; Peng, F.; Zhang, P. Recent Advances in Metal Sulfides: From Controlled Fabrication to Electrocatalytic, Photocatalytic and Photoelectrochemical Water Splitting and Beyond. *Chem. Soc. Rev.* **2019**, *48*, 4178–4280. [CrossRef]
4. Zheng, X.-L.; Yang, Y.-J.; Liu, Y.-H.; Deng, P.-L.; Li, J.; Liu, W.-F.; Rao, P.; Jia, C.-M.; Huang, W.; Du, Y.-L.; et al. Fundamentals and Photocatalytic Hydrogen Evolution Applications of Quaternary Chalcogenide Semiconductor: Cu₂ZnSnS₄. *Rare Met.* **2022**, *41*, 2153–2168. [CrossRef]
5. Lin, L.; Yu, Z.; Wang, X. Crystalline Carbon Nitride Semiconductors for Photocatalytic Water Splitting. *Angew. Chem. Int. Ed. Engl.* **2019**, *58*, 6164–6175. [CrossRef] [PubMed]
6. Cai, H.; Wang, B.; Xiong, L.; Bi, J.; Hao, H.; Yu, X.; Li, C.; Liu, J.; Yang, S. Boosting Photocatalytic Hydrogen Evolution of g-C₃N₄ Catalyst Via Lowering the Fermi Level of Co-Catalyst. *Nano Res.* **2021**, *15*, 1128–1134. [CrossRef]
7. Hainer, A.S.; Hodgins, J.S.; Sandre, V.; Vallieres, M.; Lanterna, A.E.; Scaiano, J.C. Photocatalytic Hydrogen Generation Using Metal-Decorated TiO₂: Sacrificial Donors Vs True Water Splitting. *ACS Energy Lett.* **2018**, *3*, 542–545. [CrossRef]

8. Chun, W.-J.; Ishikawa, A.; Fujisawa, H.; Takata, T.; Kondo, J.N.; Hara, M.; Kawai, M.; Matsumoto, Y.; Domen, K. Conduction and Valence Band Positions of Ta₂O₅, TaON, and Ta₃N₅ by Ups and Electrochemical Methods. *J. Phys. Chem. B* **2003**, *107*, 1798–1803. [[CrossRef](#)]
9. Qiu, J.-Y.; Feng, H.-Z.; Chen, Z.-H.; Ruan, S.-H.; Chen, Y.-P.; Xu, T.-T.; Su, J.-Y.; Ha, E.-N.; Wang, L.-Y. Selective Introduction of Surface Defects in Anatase TiO₂ Nanosheets for Highly Efficient Photocatalytic Hydrogen Generation. *Rare Met.* **2022**, *41*, 2074–2083. [[CrossRef](#)]
10. Sun, L.-J.; Su, H.-W.; Xu, D.-F.; Wang, L.-L.; Tang, H.; Liu, Q.-Q. Carbon Hollow Spheres as Cocatalyst of Cu-Doped TiO₂ Nanoparticles for Improved Photocatalytic H₂ Generation. *Rare Met.* **2022**, *41*, 2063–2073. [[CrossRef](#)]
11. Ma, Z.; Li, P.; Ye, L.; Wang, L.; Xie, H.; Zhou, Y. Selectivity Reversal of Photocatalytic CO₂ Reduction by Pt Loading. *Catal. Sci. Technol.* **2018**, *8*, 5129–5132. [[CrossRef](#)]
12. Yi, S.-S.; Zhang, X.-B.; Wulan, B.-R.; Yan, J.-M.; Jiang, Q. Non-Noble Metals Applied to Solar Water Splitting. *Energy Environ. Sci.* **2018**, *11*, 3128–3156. [[CrossRef](#)]
13. Wang, P.; Zong, L.; Guan, Z.; Li, Q.; Yang, J. Pt_{ni} Alloy Cocatalyst Modification of Eosin Y-Sensitized g-C₃N₄/Go Hybrid for Efficient Visible-Light Photocatalytic Hydrogen Evolution. *Nanoscale Res. Lett.* **2018**, *13*, 33. [[CrossRef](#)] [[PubMed](#)]
14. Wang, S.; Xiong, L.; Bi, J.; Zhang, X.; Yang, G.; Yang, S. Structural and Electronic Stabilization of Pt_{ni} Concave Octahedral Nanoparticles by P Doping for Oxygen Reduction Reaction in Alkaline Electrolytes. *ACS Appl. Mater. Interfaces* **2018**, *10*, 27009–27018. [[CrossRef](#)] [[PubMed](#)]
15. Jiang, S.; Ma, Y.; Jian, G.; Tao, H.; Wang, X.; Fan, Y.; Lu, Y.; Hu, Z.; Chen, Y. Facile Construction of Pt-Co/CN_x Nanotube Electrocatalysts and Their Application to the Oxygen Reduction Reaction. *Adv. Mater.* **2009**, *21*, 4953–4956. [[CrossRef](#)] [[PubMed](#)]
16. Han, S.; Yun, Q.; Tu, S.; Zhu, L.; Cao, W.; Lu, Q. Metallic Ruthenium-Based Nanomaterials for Electrocatalytic and Photocatalytic Hydrogen Evolution. *J. Mater. Chem. A* **2019**, *7*, 24691–24714. [[CrossRef](#)]
17. Xing, B.; Wang, T.; Zheng, Z.; Liu, S.; Mao, J.; Li, C.; Li, B. Synchronous Fabrication of Ru Single Atoms and RuO₂ on Hierarchical TiO₂ Spheres for Enhanced Photocatalytic Coproduction of H₂ and Benzaldehyde. *Chem. Eng. J.* **2023**, *461*, 141871. [[CrossRef](#)]
18. Zhang, J.; Xu, X.; Yang, L.; Cheng, D.; Cao, D. Single-Atom Ru Doping Induced Phase Transition of MoS₂ and S Vacancy for Hydrogen Evolution Reaction. *Small Methods* **2019**, *3*, 1900653. [[CrossRef](#)]
19. Jiao, J.; Zhang, N.N.; Zhang, C.; Sun, N.; Pan, Y.; Chen, C.; Li, J.; Tan, M.; Cui, R.; Shi, Z.; et al. Doping Ruthenium into Metal Matrix for Promoted Ph-Universal Hydrogen Evolution. *Adv. Sci.* **2022**, *9*, e2200010. [[CrossRef](#)]
20. Boronat, M.; Leyva-Perez, A.; Corma, A. Theoretical and Experimental Insights into the Origin of the Catalytic Activity of Subnanometric Gold Clusters: Attempts to Predict Reactivity with Clusters and Nanoparticles of Gold. *Acc. Chem. Res.* **2014**, *47*, 834–844. [[CrossRef](#)]
21. Flytzani-Stephanopoulos, M.; Gates, B.C. Atomically Dispersed Supported Metal Catalysts. *Annu. Rev. Chem. Biomol. Eng.* **2012**, *3*, 545–574. [[CrossRef](#)]
22. Tahir, B.; Tahir, M. Synergistic Effect of Ru Embedded 2D Ti₃AlC₂ Binary Cocatalyst with Porous g-C₃N₄ to Construct 2D/2D Ru-MAX/PCN Heterojunction for Enhanced Photocatalytic H₂ Production. *Mater. Res. Bull.* **2021**, *144*, 111493. [[CrossRef](#)]
23. Yi, W.-J.; Du, X.; Zhang, M.; Yi, S.-S.; Xia, R.-H.; Li, C.-Q.; Liu, Y.; Liu, Z.-Y.; Zhang, W.-L.; Yue, X.-Z. Rational Distribution of Ru Nanodots on 2D Ti_{3-x}C₂T_y/g-C₃N₄ Heterostructures for Boosted Photocatalytic H₂ Evolution. *Nano Res.* **2023**, *16*, 6652–6660. [[CrossRef](#)]
24. Zheng, Y.; Jiao, Y.; Chen, J.; Liu, J.; Liang, J.; Du, A.; Zhang, W.; Zhu, Z.; Smith, S.C.; Jaroniec, M.; et al. Nanoporous Graphitic-C₃N₄@Carbon Metal-Free Electrocatalysts for Highly Efficient Oxygen Reduction. *J. Am. Chem. Soc.* **2011**, *133*, 20116–20119. [[CrossRef](#)]
25. Zhang, X.; Yuan, X.; Jiang, L.; Zhang, J.; Yu, H.; Wang, H.; Zeng, G. Powerful Combination of 2D g-C₃N₄ and 2D Nanomaterials for Photocatalysis: Recent Advances. *Chem. Eng. J.* **2020**, *390*, 124475. [[CrossRef](#)]
26. Tang, Y.; Yang, C.; Xu, X.; Kang, Y.; Henzie, J.; Que, W.; Yamauchi, Y. Mxene Nanoarchitectonics: Defect-Engineered 2D Mxenes Towards Enhanced Electrochemical Water Splitting. *Adv. Energy Mater.* **2022**, *12*, 2103867. [[CrossRef](#)]
27. Ou, M.; Tu, W.; Yin, S.; Xing, W.; Wu, S.; Wang, H.; Wan, S.; Zhong, Q.; Xu, R. Amino-Assisted Anchoring of CsPbBr₃ Perovskite Quantum Dots on Porous g-C₃N₄ for Enhanced Photocatalytic CO₂ Reduction. *Angew. Chem. Int. Ed. Engl.* **2018**, *57*, 13570–13574. [[CrossRef](#)]
28. Liu, W.; Zhang, D.; Wang, R.; Zhang, Z.; Qiu, S. 2D/2D Interface Engineering Promotes Charge Separation of Mo₂C/g-C₃N₄ Nanojunction Photocatalysts for Efficient Photocatalytic Hydrogen Evolution. *ACS Appl. Mater. Interfaces* **2022**, *14*, 31782–31791. [[CrossRef](#)]
29. Gao, L.; Liu, J.; Long, H.; Wang, P.; Yu, H. One-Step Calcination Synthesis of WC–Mo₂C Heterojunction Nanoparticles as Novel H₂-Production Cocatalysts for Enhanced Photocatalytic Activity of TiO₂. *Catal. Sci. Technol.* **2021**, *11*, 7307–7315. [[CrossRef](#)]
30. Kim, S.; Choi, C.; Hwang, J.; Park, J.; Jeong, J.; Jun, H.; Lee, S.; Kim, S.K.; Jang, J.H.; Jung, Y.; et al. Interaction Mediator Assisted Synthesis of Mesoporous Molybdenum Carbide: Mo-Valence State Adjustment for Optimizing Hydrogen Evolution. *ACS Nano* **2020**, *14*, 4988–4999. [[CrossRef](#)]
31. Liu, J.; Wang, P.; Fan, J.; Yu, H.; Yu, J. Hetero-Phase MoC–Mo₂C Nanoparticles for Enhanced Photocatalytic H₂-Production Activity of TiO₂. *Nano Res.* **2020**, *14*, 1095–1102. [[CrossRef](#)]
32. Pan, M.; Wang, P.; Wang, X.; Chen, F.; Yu, H. Weakening Mo–H Bond of Mo₂C Mxene Cocatalyst by Increased Antibonding-Orbital Occupancy State for Superior Photocatalytic Hydrogen Production. *ACS Sustain. Chem. Eng.* **2023**, *11*, 13222–13231. [[CrossRef](#)]

33. Wu, Y.; Wang, L.; Bo, T.; Chai, Z.; Gibson, J.K.; Shi, W. Boosting Hydrogen Evolution in Neutral Medium by Accelerating Water Dissociation with Ru Clusters Loaded on Mo₂CT_x Mxene. *Adv. Funct. Mater.* **2023**, *33*, 2214375. [[CrossRef](#)]
34. Ong, W.-J.; Tan, L.-L.; Chai, S.-P.; Yong, S.-T.; Mohamed, A.R. Surface Charge Modification Via Protonation of Graphitic Carbon Nitride (g-C₃N₄) for Electrostatic Self-Assembly Construction of 2D/2D Reduced Graphene Oxide (rGO)/g-C₃N₄ Nanostructures toward Enhanced Photocatalytic Reduction of Carbon Dioxide to Methane. *Nano Energy* **2015**, *13*, 757–770. [[CrossRef](#)]
35. Lei, C.; Zhou, W.; Shen, L.; Zheng, X.; Feng, Q.; Liu, Y.; Lei, Y.; Liang, S.; Zhang, D.; Jiang, L.; et al. Enhanced Selective H₂S Oxidation Performance on Mo₂C-Modified g-C₃N₄. *ACS Sustain. Chem. Eng.* **2019**, *7*, 16257–16263. [[CrossRef](#)]
36. Zhang, M.; Chen, J.; Li, H.; Cai, P.; Li, Y.; Wen, Z. Ru-RuO₂/CNT Hybrids as High-Activity PH-Universal Electrocatalysts for Water Splitting within 0.73 V in an Asymmetric-Electrolyte Electrolyzer. *Nano Energy* **2019**, *61*, 576–583. [[CrossRef](#)]
37. Yang, Q.; Wang, T.; Zheng, Z.; Xing, B.; Li, C.; Li, B. Constructing Interfacial Active Sites in Ru/g-C₃N_{4-x} Photocatalyst for Boosting H₂ Evolution Coupled with Selective Benzyl-Alcohol Oxidation. *Appl. Catal. B Environ.* **2022**, *315*, 121575. [[CrossRef](#)]
38. Zhao, Y.; Kamiya, K.; Hashimoto, K.; Nakanishi, S. In Situ CO₂-Emission Assisted Synthesis of Molybdenum Carbonitride Nanomaterial as Hydrogen Evolution Electrocatalyst. *J. Am. Chem. Soc.* **2015**, *137*, 110–113. [[CrossRef](#)] [[PubMed](#)]
39. Ma, R.; Zhou, Y.; Chen, Y.; Li, P.; Liu, Q.; Wang, J. Ultrafine Molybdenum Carbide Nanoparticles Compositing with Carbon as a Highly Active Hydrogen-Evolution Electrocatalyst. *Angew. Chem. Int. Ed. Engl.* **2015**, *54*, 14723–14727. [[CrossRef](#)]
40. Alex, C.; Jana, R.; Ramakrishnan, V.; Naduvil Kovilakath, M.S.; Datta, A.; John, N.S.; Tayal, A. Probing the Evolution of Active Sites in MoO₂ for Hydrogen Generation in Acidic Medium. *ACS Appl. Energy Mater.* **2023**, *6*, 5342–5351. [[CrossRef](#)]
41. Borgschulte, A.; Sambalova, O.; Delmelle, R.; Jenatsch, S.; Hany, R.; Nuesch, F. Hydrogen Reduction of Molybdenum Oxide at Room Temperature. *Sci. Rep.* **2017**, *7*, 40761. [[CrossRef](#)] [[PubMed](#)]
42. Zou, Y.; Ma, D.; Sun, D.; Mao, S.; He, C.; Wang, Z.; Ji, X.; Shi, J.-W. Carbon Nanosheet Facilitated Charge Separation and Transfer between Molybdenum Carbide and Graphitic Carbon Nitride toward Efficient Photocatalytic H₂ Production. *Appl. Surf. Sci.* **2019**, *473*, 91–101. [[CrossRef](#)]
43. Yang, Y.; Qian, Y.; Luo, Z.; Li, H.; Chen, L.; Cao, X.; Wei, S.; Zhou, B.; Zhang, Z.; Chen, S.; et al. Water Induced Ultrathin Mo₂C Nanosheets with High-Density Grain Boundaries for Enhanced Hydrogen Evolution. *Nat. Commun.* **2022**, *13*, 7225. [[CrossRef](#)] [[PubMed](#)]
44. Li, B.; Song, H.; Han, F.; Wei, L. Photocatalytic Oxidative Desulfurization and Denitrogenation for Fuels in Ambient Air over Ti₃C₂/g-C₃N₄ Composites under Visible Light Irradiation. *Appl. Catal. B Environ.* **2020**, *269*, 118845. [[CrossRef](#)]
45. Su, T.; Hood, Z.D.; Naguib, M.; Bai, L.; Luo, S.; Rouleau, C.M.; Ivanov, I.N.; Ji, H.; Qin, Z.; Wu, Z. 2D/2D Heterojunction of Ti₃C₂/g-C₃N₄ Nanosheets for Enhanced Photocatalytic Hydrogen Evolution. *Nanoscale* **2019**, *11*, 8138–8149. [[CrossRef](#)] [[PubMed](#)]
46. Cheng, C.; Zong, S.; Shi, J.; Xue, F.; Zhang, Y.; Guan, X.; Zheng, B.; Deng, J.; Guo, L. Facile Preparation of Nanosized Mop as Cocatalyst Coupled with g-C₃N₄ by Surface Bonding State for Enhanced Photocatalytic Hydrogen Production. *Appl. Catal. B Environ.* **2020**, *265*, 118620. [[CrossRef](#)]
47. Yan, Z.; Wang, W.; Du, L.; Zhu, J.; Phillips, D.L.; Xu, J. Interpreting the Enhanced Photoactivities of 0d/1d Heterojunctions of CdS Quantum Dots/TiO₂ Nanotube Arrays Using Femtosecond Transient Absorption Spectroscopy. *Appl. Catal. B Environ.* **2020**, *275*, 119151. [[CrossRef](#)]
48. Zhang, W.; Xu, C.; Liu, E.; Fan, J.; Hu, X. Facile Strategy to Construct Z-Scheme ZnCo₂O₄/g-C₃N₄ Photocatalyst with Efficient H₂ Evolution Activity. *Appl. Surf. Sci.* **2020**, *515*, 146039. [[CrossRef](#)]
49. He, F.; Chen, G.; Zhou, Y.; Yu, Y.; Li, L.; Hao, S.; Liu, B. ZIF-8 Derived Carbon (C-ZIF) as a Bifunctional Electron Acceptor and Her Cocatalyst for g-C₃N₄: Construction of a Metal-Free, All Carbon-Based Photocatalytic System for Efficient Hydrogen Evolution. *J. Mater. Chem. A* **2016**, *4*, 3822–3827. [[CrossRef](#)]
50. Che, H.; Liu, C.; Che, G.; Liao, G.; Dong, H.; Li, C.; Song, N.; Li, C. Facile Construction of Porous Intramolecular g-C₃N₄-Based Donor-Acceptor Conjugated Copolymers as Highly Efficient Photocatalysts for Superior H₂ Evolution. *Nano Energy* **2020**, *67*, 104273. [[CrossRef](#)]
51. Boppella, R.; Yang, W.; Tan, J.; Kwon, H.-C.; Park, J.; Moon, J. Black Phosphorus Supported Ni₂P Co-Catalyst on Graphitic Carbon Nitride Enabling Simultaneous Boosting Charge Separation and Surface Reaction. *Appl. Catal. B Environ.* **2019**, *242*, 422–430. [[CrossRef](#)]
52. Zhou, X.; Tian, Y.; Luo, J.; Jin, B.; Wu, Z.; Ning, X.; Zhan, L.; Fan, X.; Zhou, T.; Zhang, S.; et al. MoC Quantum Dots@N-Doped-Carbon for Low-Cost and Efficient Hydrogen Evolution Reaction: From Electrocatalysis to Photocatalysis. *Adv. Funct. Mater.* **2022**, *32*, 2201518. [[CrossRef](#)]
53. Huang, Z.; Long, X.; Liu, M.; Li, X.; Du, Y.; Liu, Q.; Chen, Y.; Guo, S.; Chen, R. Constructing CoP-C/g-C₃N₄ Nanocomposites with P-C Bond Bridged Interface and Van Der Waals Heterojunctions for Enhanced Photocatalytic H₂ Evolution. *J. Colloid Interface Sci.* **2024**, *653*, 1293–1303. [[CrossRef](#)] [[PubMed](#)]
54. Dong, J.; Shi, Y.; Huang, C.; Wu, Q.; Zeng, T.; Yao, W. A New and stable Mo-Mo₂C modified g-C₃N₄ photocatalyst for efficient visible light photocatalytic H₂ production. *Appl. Catal. B Environ.* **2019**, *243*, 27–35. [[CrossRef](#)]
55. Zhang, J.; Wu, M.; He, B.; Wang, R.; Wang, H.; Gong, Y. Facile synthesis of rod-like g-C₃N₄ by decorating Mo₂C co-catalyst for enhanced visible-light photocatalytic activity. *Applied Surface Science* **2019**, *470*, 565–572. [[CrossRef](#)]
56. Liu, R.-Y.; Ding, L.; Yang, G.-D.; Zhang, J.-Y.; Jiao, R.; Sun, H.-Z. Hollow Mo₂C nanospheres modified B-doped g-C₃N₄ for high efficient photocatalysts. *J. Phys. D Appl. Phys.* **2022**, *55*, 454001. [[CrossRef](#)]

57. Du, J.; Shen, Y.; Yang, F.; Zhang, B.; Jiang, X.; An, C.; Ye, J. In situ construction of an α -Mo₂C/g-C₃N₄ Mott–Schottky heterojunction with high-speed electron transfer channel for efficient photocatalytic H₂ evolution. *Inorg. Chem. Front.* **2023**, *10*, 832–840. [[CrossRef](#)]
58. Song, Y.; Xia, K.; Gong, Y.; Chen, H.; Li, L.; Yi, J.; She, X.; Chen, Z.; Wu, J.; Li, H.; et al. Controllable synthesized heterostructure photocatalyst Mo₂C@C/2D g-C₃N₄: Enhanced catalytic performance for hydrogen production. *Dalton Trans.* **2018**, *47*, 14706–14712. [[CrossRef](#)]
59. Tan, X.Q.; Zhang, P.; Chen, B.; Mohamed, A.R.; Ong, W.J. Synergistic effect of dual phase cocatalysts: MoC-Mo₂C quantum dots anchored on g-C₃N₄ for high-stability photocatalytic hydrogen evolution. *J. Colloid Interface Sci.* **2024**, *662*, 870–882. [[CrossRef](#)]

Disclaimer/Publisher’s Note: The statements, opinions and data contained in all publications are solely those of the individual author(s) and contributor(s) and not of MDPI and/or the editor(s). MDPI and/or the editor(s) disclaim responsibility for any injury to people or property resulting from any ideas, methods, instructions or products referred to in the content.